Biomaterials Science

Accepted Manuscript

This article can be cited before page numbers have been issued, to do this please use: Y. Hu, F. Zhang, L. Chen, X. Xu, P. Zhang, Y. Li, J. Fan, J. Zou and Y. Zhao, *Biomater. Sci.*, 2025, DOI: 10.1039/D5BM00954E.

ROYAL SOCIETY OF CHEMISTRY

rsc.li/biomaterials-science

View Article Online
DOI: 10.1039/D5BM00954E

ARTICLE

Composite Nano Copper Carrier Combined Cuproptosis and Photodynamic Therapy for Spatiotemporal Synergistic Anti-Tumor

Received 00th January 20xx,
Accepted 00th January 20xx

DOI: 10.1039/x0xx00000x

Yong-Guo Hu[a, ‡], Fang Zhang[a, ‡], Li-Li Chen[a,‡], Xin-Yue Xu[a], Pei-Jie Zhang[a], Yong Li [a], Jin-Xuan Fan[a], Jia-Hua Zou[a, b, c, *] and Yuan-Di Zhao[a, *]

Cuproptosis is a copper-dependent programmed cell death triggered by mitochondrial dysfunction, offers significant anti-tumor potential but requires tumor-specific copper delivery to avoid systemic toxicity. Here, we developed a synergistic nanoplatform (Cu_2O@SiO_2-Ce6, CSC) integrating cuproptosis induction with photodynamic therapy (PDT). Cuprous oxide (Cu_2O) core was encapsulated in silicon dioxide and covalently linked to the photosensitizer Ce6. After accumulating in tumors regions via the EPR effect, CSC releases a surge of copper ions upon encountering the acidic tumor microenvironment and lysosomes. These ions induce mitochondrial cuproptosis by aggregating lipoylated TCA cycle proteins and depleting Fe-S cluster proteins. Concurrently, laser irradiation activates Ce6 to generate cytotoxic reactive oxygen species (ROS), actively disrupting tumor membranes. The experiments showed that the nanoplatform significantly enhanced the tumor cell killing effect and reduced the toxicity to normal tissues through a dual mechanism, which provided a new strategy for overcoming the drug resistance of PDT and the precise regulation of cuproptosis.

Introduction

Programmed cell death such as apoptosis, necrosis and ferroptosis serves as a precise and effective therapeutic strategy for eliminating tumor cells during cancer treatment[1, 2]. Each programmed cell death pathway exhibits distinct biological features that can be exploited for targeted treatment. For instance, apoptotic tumor cells can induce a bystander effect, sensitizing adjacent cells to chemotherapeutic agents[3, 4]. Pyroptotic cells undergo rapid release of tumor-associated antigens, potentiating tumor-specific immune responses[5, 6]. Cuproptosis is a newly identified form of programmed cell death triggered by mitochondrial dysfunction[7]. In humans, copper serves as an essential trace element, with balanced copper homeostasis regulating numerous biochemical reactions to maintain normal physiological functions[8, 9]. However, upon entering mitochondria, excess copper binds to ferredoxin 1 (FDX1) as a substrate, undergoing reduction to cuprous ions (Cu^+) before being released[10]. FDX1 and lipoic acid synthetase (LIAS) can catalyze lipoylated dihydrolipoamide S-acetyltransferase (DLAT) in the mitochondria. On the one hand, Cu^+ can bind to DLAT, the "switch" that allows pyruvate to enter the mitochondria becomes dysfunctional, resulting in severe inhibition of the entire TCA cycle due to the lack of substrate. On the other hand, its reduced synthesis of the Fe-S cluster, which plays various roles in mitochondria, including as cofactors for respiratory enzyme complexes (I–III), involvement in lipoic acid synthesis, and biosynthesis of heme[11]. The combined action of both ultimately leads to cell death. This unique programmed cell death mechanism can further elicit robust immune responses, not only kill tumor cells but also activate immune cells for long-term eradication of residual cancer cells[12, 13]. Notably, cuproptosis may occur in both normal and malignant cells, creating an urgent need to develop strategies that enhance drug accumulation specifically in tumor tissues while minimizing damage to healthy tissues.

Nano copper carriers can significantly enhance tumor-specific copper accumulation[14]. Representative copper-containing nanoplatform, such as copper sulfide (CuS) and cuprous oxide (Cu_2O)[15-20], serve as excellent delivery vehicles that not only carry substantial amounts of copper but also effectively mask its ionic toxicity through their stable nanostructures. The aberrant vascular architecture of tumor tissue enables nanoplatform (typically 10-200 nm in size) to extravasate through the vessel walls and accumulate preferentially in tumor sites via the enhanced permeability and retention (EPR) effect[21, 22]. Under the acidic stimulation of the tumor microenvironment and lysosomes, these nanostructures undergo degradation, releasing a surge of copper ions that rapidly elevate intracellular concentrations, thereby inducing acute cuproptosis. Copper-based nanoplatforms represent a highly promising cuproptosis-mediated antitumor strategy by precisely disrupting copper ion homeostasis to induce tumor-specific cuproptosis[23-25]. Notably, these nanoplatforms exhibit versatile physicochemical properties, including adjustable nanostructures and high chemical modifiability. Through rational integration of therapeutic agents (e.g., chemotherapeutics, photosensitizers, and immune adjuvants), they can synergize cuproptosis with chemotherapy,

[a.] *Britton Chance Center for Biomedical Photonics at Wuhan National Laboratory for Optoelectronics Hubei Bioinformatics & Molecular Imaging Key Laboratory, Department of Biomedical Engineering, College of Life Science and Technology, Huazhong University of Science and Technology, Wuhan, 430074, Hubei, P. R. China. Email address: zydi@mail.hust.edu.cn (Y.-D. Zhao)*
[b.] *Department of Oncology, Huanggang Central Hospital of Yangtze University, No.126 Qi'an Road, Huangzhou District, Huanggang City 438000, Hubei, P.R. China. Email address: zoujiahua@hgyy.org.cn (J.-H. Zou)*
[c.] *Hubei Clinical Medical Research Center of Esophageal and Gastric Malignancy, Huanggang City 438021, Hubei, P.R. China*
‡These authors contributed equally to this work
†Supplementary Information (SI) available: See DOI: 10.1039/x0xx00000x

photodynamic therapy, and immunotherapy, thereby significantly enhancing antitumor efficacy.

Photodynamic therapy (PDT) is an anticancer modality that employs external light activation of photosensitizers to generate cytotoxic reactive oxygen species (ROS)[26-32]. Chlorin e6 (Ce6), a widely used photosensitizer in PDT, demonstrates favorable therapeutic characteristics including reduced phototoxicity and high-efficiency singlet oxygen ($^1O_2$) generation under red light irradiation, making it clinically valuable for oncological applications[33-36]. The therapeutic efficacy of PDT stems from direct ROS-mediated cytotoxicity. However, the clinical application of PDT faces significant challenges, particularly the development of resistance mechanisms that limit its long-term effectiveness. Tumor cells can develop PDT resistance through multiple pathways, including upregulation of antioxidant systems (e.g., activation of hypoxia-inducible factor-1α (HIF-1α) under low-oxygen conditions[37], and enhanced DNA repair mechanisms[38]. To overcome these limitations, innovative strategies such as nanoparticle-based oxygen carriers[39], ROS-amplifying agents[40], and combination therapies with immune checkpoint inhibitors[41] have been explored. Notably, the integration of PDT with cuproptosis—a novel copper-dependent cell death pathway—has shown promise in bypassing traditional resistance mechanisms by inducing mitochondrial protein aggregation and proteotoxic stress. The strategic combination of PDT with cuproptosis induction creates a dual "active-passive" therapeutic paradigm that synergistically enhances antitumor efficacy through complementary mechanisms. As demonstrated in Figure 1, we developed a cuprous oxide (Cu_2O) nanoplatform-based theranostic probe (denoted as $Cu_2O@SiO_2$-Ce6, CSC) that synergistically integrates cuproptosis induction with photodynamic therapy. Specifically, we engineered a silica shell-coated cuprous oxide nanoplatform ($Cu_2O@SiO_2$), with the photosensitizer Ce6 conjugated to the shell surface via amide bonds. The CSC nanoplatform preferentially accumulate at tumor sites through the enhanced permeability and retention (EPR) effect. Upon external laser irradiation, Ce6 generates abundant reactive oxygen species (ROS) that disrupt tumor cell membrane integrity. Simultaneously, under the acidic stimulation of the tumor microenvironment and lysosomes, the cuprous oxide (Cu_2O) nanoplatform undergo structural degradation, releasing abundant copper ions. These ions subsequently enter mitochondria and bind to lipoylated proteins in the tricarboxylic acid (TCA) cycle, inducing protein aggregation. This process leads to iron-sulfur cluster protein (Fe-S protein) depletion, triggering proteotoxic stress and ultimately resulting in cell death, thereby achieving synergistic tumor treatment through combined photodynamic therapy and cuproptosis. Both in vitro and in vivo experimental results demonstrate that this integrated nanotherapeutic platform effectively inhibits tumor cell growth while maintaining excellent biosafety in normal tissues. This work provides a significant conceptual advance for multimodal synergistic cancer therapy.

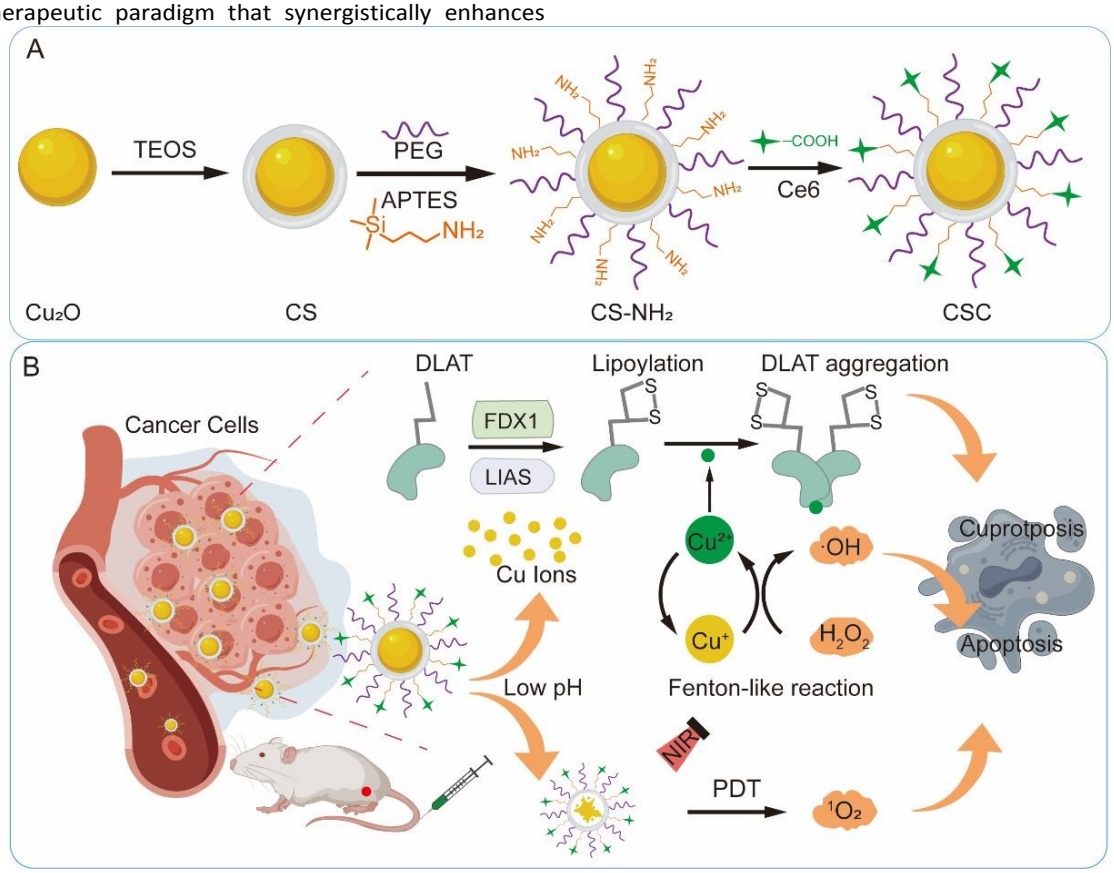

Figure 1. Synthesis and antitumor mechanism of CSC. (A) Schematic illustration of synthesis of CSC and (B) its application for photodynamic-enhanced cuproptosis-apoptosis synergistic tumor therapy.

View Article Online
DOI: 10.1039/D5BM00954E

ARTICLE

Results and Discussion

Synthesis and Characterization of CSC

In this paper, we prepared Cu_2O nanoplatform by reduction of copper hydroxide with ascorbic acid using PVP as surfactant[42, 43]. Cu_2O is inherently unstable and prone to oxidation, but SiO_2 coating not only significantly enhances its stability[44] but also facilitates further modification[45]. Functionalization with mPEG-silane and APTES (γ-aminopropyltriethoxysilane), improves nanoparticle stability, reduces off-target toxicity, and promotes tumor accumulation through EPR effect[46], while providing anchoring sites for the Ce6[47]. TEOS was hydrolyzed under alkaline environment to form SiO_2, which was uniformly coated on the surface of Cu_2O particles ($Cu_2O@SiO_2$, CS), and after surface modification with APTES, the surface of CS carries a large number of amino groups ($Cu_2O@SiO_2$-NH_2, CS-NH_2). The carboxyl groups in the photosensitizer Ce6 were covalently attached to the aminated silica surface ($Cu_2O@SiO_2$-Ce6, CSC) via amide bonds. To verify the successful preparation of the nanoparticles, we first characterized them using transmission electron microscopy (TEM). As shown in Figure 2A, the TEM images demonstrate that Cu_2O, CS, and CSC are uniformly dispersed with homogeneous particle sizes. The Cu_2O particles exhibit a cubic morphology with an approximate size of 80 nm. Both CS and CSC nanoplatform are around 100 nm in diameter and display a distinct core-shell structure, where the Cu_2O core is enveloped by an approximately 10 nm-thick outer SiO_2 shell. This confirms the successful coating of silica on the Cu_2O surface without altering its morphology or size. Compared with CS, the CSC conjugated with Ce6 shows no significant changes in either morphology or particle size. These results indicate the successful preparation of Cu_2O, CS, and CSC nanoplatforms. Cu_2O exhibits pH-responsive characteristics, being prone to degradation under acidic conditions (pH = 6.5) while remaining relatively stable in a neutral environment (pH = 7.4).

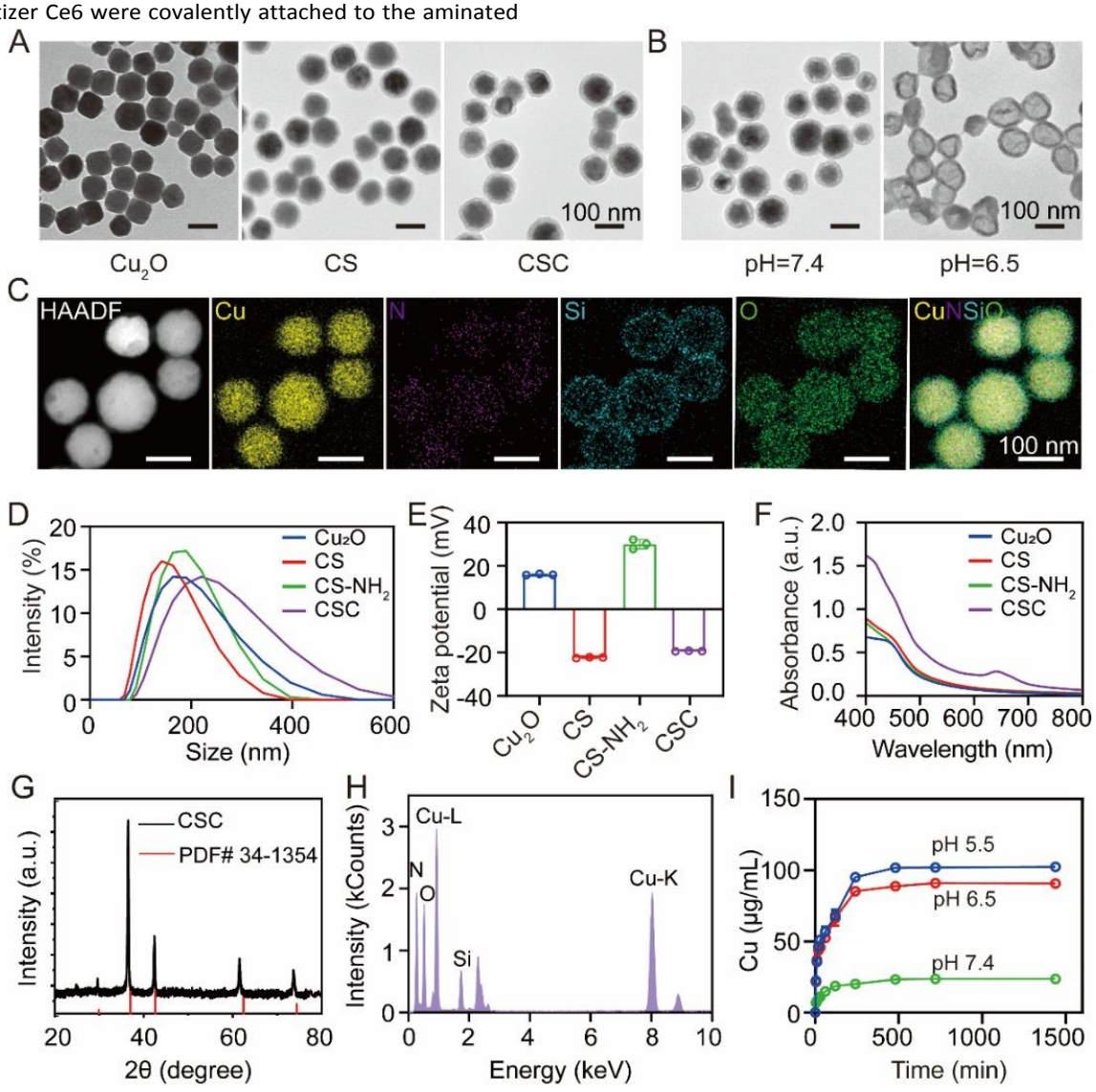

View Article Online
DOI: 10.1039/D5BM00954E

Figure 2. Characterization of the physicochemical properties of the probes. (A) Transmission electron microscopy (TEM) images of Cu_2O, CS and CSC. Scale bar: 100 nm. (B) TEM images of CSC at pH = 7.4 and pH = 6.5. Scale bar: 100 nm. (C) Element mapping image of CSC. (D) Hydrated particle sizes and (E) zeta potentials of Cu_2O, CS, CS-NH_2 and CSC. Data are presented as the means ± SD. (n = 3 independent samples). (F) UV-vis absorption spectra of Cu_2O, CS, CS-NH_2 and CSC. (G) XRD of Cu_2O, CS, CS-NH_2 and CSC. (H) Energy dispersive spectra (EDS) of CSC. (I) Copper ions release of CSC in PBS at different pH (n = 3 independent experiments).

To investigate whether CSC retains its pH-responsive properties after silica coating, we dispersed CSC in buffer solutions at different pH values (7.4 and 6.5) for 24 hours and subsequently characterized their morphological changes using TEM. As illustrated in Figure 2B, CSC maintained its original morphology and size at physiological pH (7.4). In contrast, under acidic conditions (pH 6.5), only the approximately 10 nm-thick SiO_2 shell remained observable, indicating that coating did not prevent the degradation of the Cu_2O core under acidic conditions. SiO_2 exhibits minimal dissolution under weakly acidic conditions[48]. This ensures controlled Cu^{2+} release primarily through pH-triggered degradation of the Cu_2O core (not SiO_2 dissolution). These results confirm that CSC maintains its pH-responsive behavior even after SiO_2 encapsulation, confirming that the SiO_2 coating did not interfere with the pH-dependent degradation of the Cu_2O core. These findings verify that the pH-responsive property of Cu_2O was preserved in the CSC nanoplatform. To further characterize the size distribution of Cu_2O, CS, and CSC nanoplatforms, dynamic light scattering (DLS) analysis was performed. As shown in Figure 2D, the hydrodynamic diameters of all three nanoplatforms predominantly ranged between 100-200 nm, which were larger than the sizes obtained by TEM. This discrepancy arises because surface charges on nanoplatforms attract polar water molecules to form ordered hydration layers. As shown in Figure S1, the CSC nanoplatform is very stable in both PBS and DMEM solutions over one week.

Furthermore, the observed variations in size among Cu_2O, CS, and CSC indicate that different surface modifications led to subtle differences in their respective hydration layers. To further characterize the differences among Cu_2O, CS, CS-NH_2, and CSC, we measured their surface charges. As shown in Figure 2E, bare Cu_2O exhibited a surface potential of approximately +15 mV, while SiO_2-coated CS showed a negative potential of -21 mV due to the presence of abundant Si-OH groups on the silica surface. After modification with (3-aminopropyl) triethoxysilane (APTES), the surface charge became positive, confirming successful introduction of amino groups. Subsequent conjugation with Ce6 through activated carboxyl groups (-COOH) neutralized part of the positive charges, while the remaining exposed -COOH groups rendered CSC negatively charged. To verify successful Ce6 conjugation, we performed UV-Vis spectroscopy analysis. As shown in Figure 2E, Cu_2O, CS, and CS-NH_2 showed no characteristic peaks between 400-800 nm, with nearly identical absorption profiles. In contrast, CSC displayed a distinct absorption peak at 660 nm corresponding to Ce6, providing conclusive evidence for successful nanoplatform functionalization. To verify whether the Cu_2O composition was altered during CSC synthesis, we conducted X-ray diffraction (XRD) analysis. As shown in Figure 2G, the XRD pattern of CSC exhibits excellent consistency with the standard Cu_2O powder diffraction file (PDF# 34-1354), confirming that the silica coating process did not modify the crystalline composition of Cu_2O. We further conducted energy-dispersive X-ray spectroscopy (EDS) analysis. As shown in Figure 2H, the CSC nanoplatform primarily consisted of Cu, Si, O, and N elements, which is consistent with the elemental mapping results. As shown in Figure S2, the XPS spectrum of Cu 2p certified that the main Cu specie was Cu^+ (Cu^+ $2p_{3/2}$: 932.55 eV and Cu^+ $2p_{1/2}$: 954.43 eV), though the few features of Cu^{2+} were also found at the binding energies of 935.27 eV (Cu^{2+} $2p_{3/2}$) and 955.06 eV (Cu^{2+} $2p_{3/2}$), which could be ascribed to oxidation. The CSC nanoplatform demonstrated excellent pH-responsive properties. We quantitatively analyzed their copper ion (Cu^{2+}) release capability under acidic conditions using atomic absorption spectroscopy. As shown in Figure 2I, the Cu^{2+} release exhibited a time- and pH-dependent increase. At pH 5.5, the cumulative Cu^{2+} release reached 102.3 ± 0.6 μg mL^{-1}, while only 23.6 ± 0.2 μg mL^{-1} was detected at physiological pH 7.4. These results clearly demonstrate the superior acid-triggered degradation capability of the CSC nanoplatform.

Cellular Uptake and Cuproptosis

The cellular uptake of nanoplatform by tumor cells plays a pivotal role in determining therapeutic efficacy, as the internalization process directly influences the effectiveness of drug delivery systems. To verify whether the nanoplatform could be internalized by cancer cells, we conducted confocal fluorescence imaging and flow cytometry experiments. 4T1 cells were co-incubated with CSC probes for varying durations (0 h, 1 h, 2 h, 4 h, and 6 h), with cell nuclei counterstained using DAPI fluorescent dye.

As shown in Figure 3A, confocal fluorescence imaging revealed distinct red fluorescence signals from Ce6-labeled CSC probes appearing in the cytoplasm after 1 h incubation. The fluorescence intensity exhibited a time-dependent enhancement, demonstrating progressive internalization of CSC nanoplatform into cells. Notably, the fluorescence signal plateaued at 4-6 h incubation periods, indicating saturation of cellular uptake capacity for CSC nanoplatform. To quantitatively assess the cellular uptake efficiency of CSC probes by 4T1 cells, flow cytometric analysis was performed. As illustrated in Figure 3B and Figure S3, the internalization rate reached 77.2% within the first hour of incubation. A time-dependent increase in nanoplatform uptake was observed, with the uptake efficiency peaking at 93.9% after 6 h of incubation, indicating near-maximal cellular internalization capacity had been achieved. Following cellular internalization, CSC release copper ions, triggering a cascade of biological effects. To validate the cuproptosis-inducing capability of CSC, we investigated the expression of cuproptosis-related proteins through Western blot analysis. 4T1 cells were treated with PBS (control), CS, or CSC, and comparative protein expression profiling was conducted to examine CSC-mediated cuproptosis. As

View Article Online
DOI: 10.1039/D5BM00954E

demonstrated in Figure 3C, both CS and CSC treatments significantly downregulated the protein levels of DLAT, ferredoxin 1 (FDX1), and lipoyl synthase (LIAS). These results confirm that CS and CSC effectively induce cuproptosis in tumor cells.

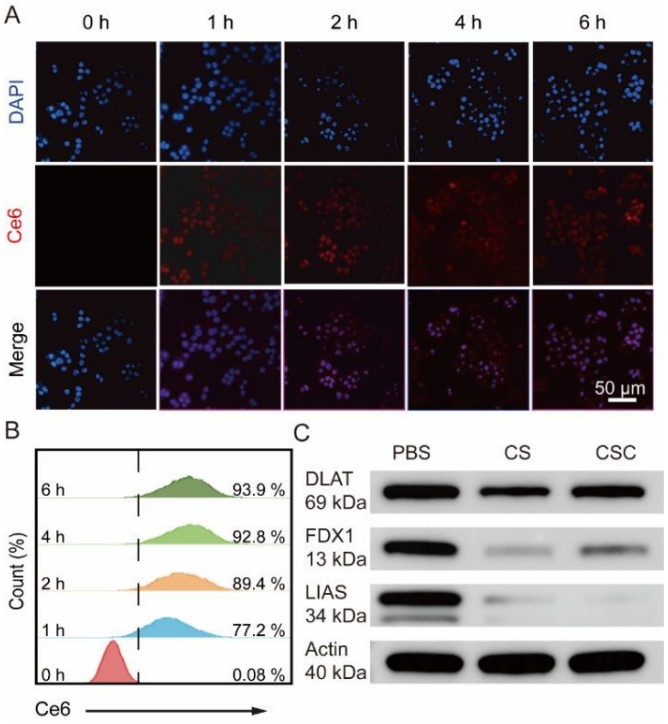

Figure 3. The uptake of CSC by tumor cell. (A) Fluorescence imaging. (B) Flow cytometry analysis and (C) DLAT, FDX1, and LIAS protein levels after treatment of 4T1 cells with different samples. The samples of the same group were derived from the same experiment, and the gels/blots were processed in parallel.

Cytotoxicity

To evaluate the cytotoxicity of CSC, NIH 3T3 and 4T1 cells were incubated with varying concentrations of CSC probes for 12 h, followed by cell viability assessment using CCK-8 assay. As shown in Figure 4A, both cell types-maintained viability above 90% at probe concentrations ranging from 0-50 μg mL^{-1}, demonstrating negligible toxicity. At 100 μg mL^{-1}, NIH 3T3 cells retained high viability (81.7±0.2%), while 4T1 cell viability decreased to 61.2±0.2%. These results indicate that CSC probes exhibit excellent biocompatibility with normal cells while demonstrating selective cytotoxicity toward tumor cells. We further evaluated the synergistic therapeutic effect of CSC (50 μg mL^{-1}) combined with photodynamic therapy on 4T1 cells. As shown in Figure 4B, laser irradiation alone showed negligible impact on cell viability, indicating minimal cellular damage from the laser treatment. Without laser irradiation, both CS and CSC probes at the same concentration induced approximately 10% cell mortality. Following laser treatment, the CS group showed no significant changes, whereas the CSC group exhibited markedly reduced cell viability. This phenomenon can be attributed to the abundant ROS generation by Ce6 in CSC probes upon laser excitation, which effectively killed tumor cells. In contrast, CS probes lacked the capacity to produce ROS under laser irradiation, resulting in lower cytotoxicity.

To further confirm ROS generation by CSC under photoexcitation, we employed 1,3-diphenylisobenzofuran (DPBF) as a molecular probe. The reaction between DPBF and ROS leads to cleavage of the furan ring, producing colorless 1,2-dibenzoylbenzene and consequently decreasing the UV-Vis absorption at 410 nm. As demonstrated in Figure 4C, the absorption loss at 410 nm progressively increased with prolonged irradiation time, indicating continuous ROS generation that oxidized DPBF. These results provide direct evidence that CSC can efficiently produce substantial ROS upon laser irradiation. To further verify intracellular ROS generation by CSC probes, we utilized 2',7'-dichlorodihydrofluorescein diacetate (DCFH-DA) as a fluorescent probe. This membrane-permeable reagent is hydrolyzed by intracellular esterases and subsequently oxidized by ROS to emit green fluorescence, with intensity proportional to ROS levels. As shown in Figure 4D, the PBS control group showed no green fluorescence regardless of laser irradiation, confirming that laser treatment alone cannot generate ROS. Both CS and CSC groups exhibited weak baseline fluorescence, potentially attributable to endogenous H_2O_2 reacting with copper ions to form ROS. Notably, laser irradiation caused no significant fluorescence enhancement in the CS group, confirming its inability to produce ROS under illumination. In contrast, the CSC group demonstrated dramatically intensified green fluorescence upon laser exposure, unequivocally demonstrating its capacity for robust ROS generation. These results collectively establish that CSC probes can effectively elevate intracellular ROS levels under laser irradiation, thereby achieving therapeutic tumor cell ablation.

To further validate the synergistic therapeutic effect of CSC probes, we performed confocal microscopy using Calcein-AM and propidium iodide (PI) on treated cells. Calcein-AM penetrates live cells and is hydrolyzed by intracellular esterases to emit green fluorescence, while PI enters membrane-compromised dead cells and binds nucleic acids to produce red fluorescence. This staining strategy enables clear differentiation between viable and dead cells. As shown in Figure 4E, PBS-treated control groups exhibited intense green fluorescence regardless of laser irradiation, confirming that laser treatment alone cannot induce cell death. Cells incubated with CS probes showed predominant green fluorescence with sporadic red signals, suggesting partial cell death potentially caused by copper ion release from internalized probes. Notably, laser irradiation failed to enhance the red fluorescence in CS groups, indicating its inability to potentiate CS-mediated cytotoxicity. In striking contrast, CSC probe-treated cells displayed dramatically different responses, laser-irradiated samples showed minimal green fluorescence but extensive red staining, indicating near-complete cell death, while non-irradiated counterparts maintained substantial viability with only scattered red signals. These results conclusively demonstrate the laser-dependent synergistic effect between copper ion release and photodynamic therapy in CSC-mediated tumor cell killing.

View Article Online
DOI: 10.1039/D5BM00954E

ARTICLE

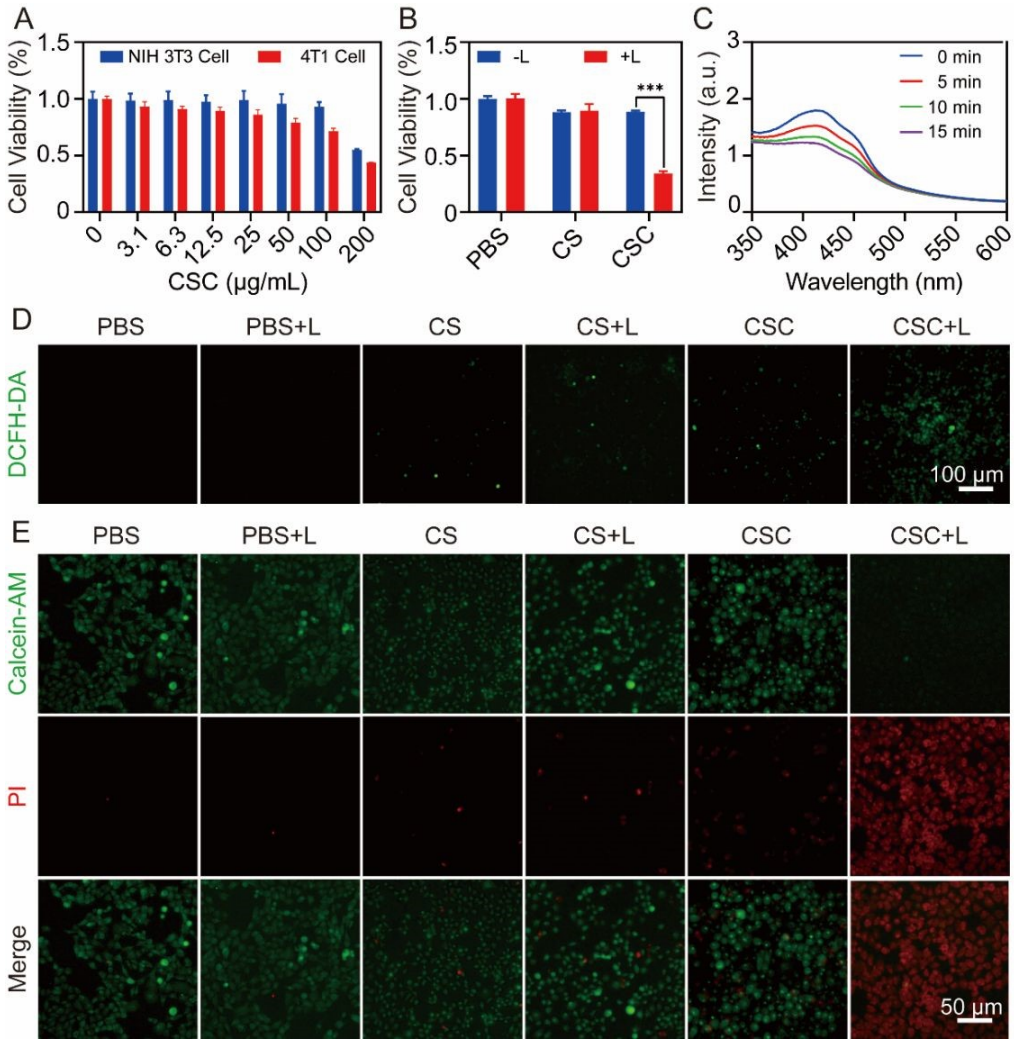

Figure 4. Cytotoxicity of nanocarrier and the production of ROS. (A) CCK-8 cytotoxicity of 4T1 and 3T3 cells incubated with different concentrations of CSC. Data were presented as the means ± SD (n = 5 independent experiments). (B) Survival rate of 4T1 cells incubated and treated with different probes, ***: p<0.01. Data were presented as the means ± SD (n = 5 independent experiments). (C) The ultraviolet–visible absorption spectra of DPBF and CSC mixed solution with different irradiation time. (D) ROS production detected by fluorescence of DCFH-DA in 4T1 cell incubated with different probes. Scale bar: 50 μm. (E) Fluorescence images of Calcein-AM/PI-stained 4T1 cell incubated with different probes under different conditions. Scale bar: 50 μm.

Biosafety Evaluation In Vivo

The biocompatibility of nanoplatform is one of the key characteristics for their application in the biomedical field, directly influencing their safety and effectiveness both in vivo and in vitro. The hemolysis assay is a critical method for evaluating their blood compatibility. Good biocompatibility requires that nanoplatform does not induce hemolytic reactions when in contact with blood components while maintaining the integrity of red blood cell membranes. Therefore, we first investigated the in vitro hemocompatibility evaluation of the nanoplatform. A total of 1.5 mL of fresh blood was collected from two 6-week-old KM mice into anticoagulant tubes. After centrifugation at 700 ×g for 5 min to remove the supernatant, the red blood cells (RBCs) were washed multiple times with PBS. Then, 10 μL of the RBC suspension was added to 400 μL of PBS containing CSC nanoplatform at concentrations of 3.2, 6.3, 12.5, 25, 50, 100, and 200 μg mL^{-1}, respectively. PBS and ultrapure water were used as the negative control and positive control, respectively. The samples were incubated at 37 °C in a 5% CO_2 incubator for 2 h, followed by centrifugation at 4000 rpm for 5 min. Photographs were taken, and the absorbance of the supernatant was measured at 577 nm. As shown in Figure S4, the hemolysis rate of red blood cells (RBCs) in ultrapure water was approximately 100%, whereas in PBS, it was nearly 0%,

View Article Online
DOI: 10.1039/D5BM00954B

which is attributed to the difference in osmotic pressure between the two solutions. When the nanoplatform was introduced into the system, the RBCs mostly settled, and the supernatant exhibited minimal changes compared to that before probe addition. Even at a high nanoplatform concentration of 200 μg mL^{-1}, the hemolysis rate remained low. These results indicate that the nanoplatform possesses excellent biocompatibility with blood cells, exerting only a negligible impact on RBCs. This finding provides a safety assurance for subsequent in vivo experiments.

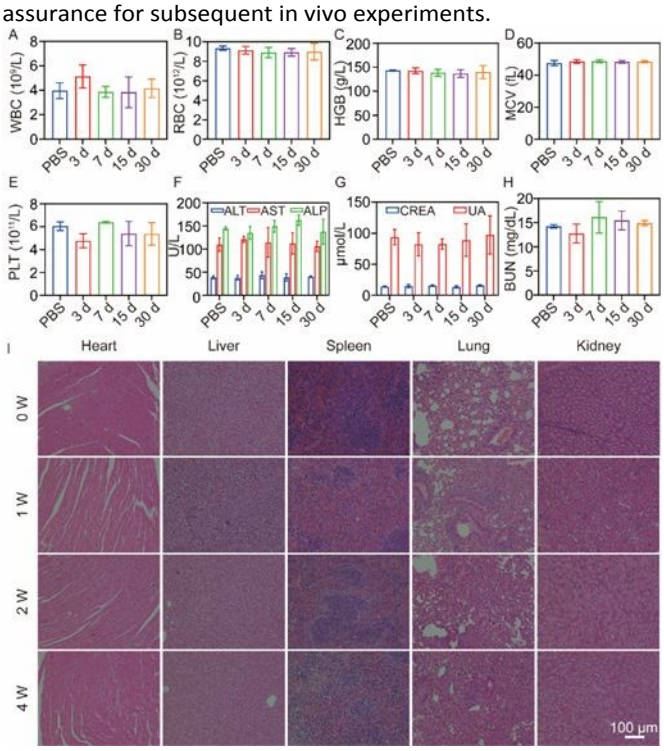

Figure 5. Blood analysis of mice after injection of CSC: (A) WBC, (B) RBC, (C) HGB, (D) MCV and (E) PLT. Liver function index analysis: (F) ALT , AST and ALP. Kidney Function index analysis: (G) CREA and UA, (H) BUN. (I) H&E staining of heart, liver, spleen, lungs, and kidneys after 1, 2 and 4 week injection of CSC. Scale bar: 100 μm.

The biocompatibility evaluation of nanoplatform requires comprehensive investigation of their effects on blood biochemical indicators, which represents a critical component of preclinical safety assessment. To determine potential in vivo toxicity, healthy mice were randomly divided into five groups (n=3 per group). CSC nanoplatform was administered via tail vein injection on 3, 7, 15, and 30 days, with one control group receiving an equivalent volume of PBS. Blood samples were collected at the endpoint of the experiment for complete biochemical analysis. As shown in Figure 5A-H, no significant differences were observed in white blood cells (WBC), red blood cells (RBC), hemoglobin (HGB), mean corpuscular volume (MCV), or platelets (PLT) between mice injected with nanoplatform on days 3, 7, 15, and 30 and the control group, demonstrating excellent hematological safety of the nanoplatform. Furthermore, key biochemical markers including alanine aminotransferase (ALT), aspartate aminotransferase (AST), alkaline phosphatase (ALP), creatinine (CREA), uric acid (UA), and blood urea nitrogen (BUN) all remained within normal ranges and showed no statistically significant differences compared to controls. These comprehensive results confirm that the nanoplatform caused no detectable hepatic or renal toxicity throughout the entire evaluation period. In addition to hematological analysis, we investigated the effects of CSC nanoplatform on mouse organs to further evaluate the biosafety of the nanoplatform. Healthy mice were randomly divided into four groups (n=3 per group). The CSC nanoplatform was administered via tail vein injection at 1, 2 and 4 weeks, with one control group receiving an equivalent volume of PBS. Upon completion of the experiment, hematoxylin-eosin staining (HE) was performed on the heart, liver, spleen, lungs and kidneys. As shown in Figure 5I, all tissue samples from mice injected with the probes at 1, 2 and 4 weeks exhibited normal and well-defined cellular morphology without pathological alterations, the myocardial cells are arranged in an orderly manner with clearly visible striations, and no ruptured or necrotic structures are observed; the liver structure shows distinct characteristic features such as hepatic lobules, with no swelling or necrotic structures present; the spleen exhibits clear splenic corpuscles with visible central arteries; the lungs display well-defined alveoli without thickening of alveolar walls, collapse, or emphysematous changes; the kidney tissue demonstrates clear structural organization with no signs of atrophy or swelling. These results demonstrate that CSC probes induce no pathological lesions in major organs, confirming their excellent biocompatibility and long-term in vivo safety. This foundational safety profile strongly supports further investigation of CSC probes for tumor therapy applications.

Tumor targeting and metabolism

Encouraged by the biocompatibility in vitro, the biodistribution in various organs and pharmacokinetics of CSC nanoplatform were further evaluated in vivo. In this experiment, Cy5.5 was first covalently conjugated to SiO_2-NH_2 via an amide bond, forming SiO_2-Cy5.5 nanoplatform (SC), similar to the method used for Ce6. Then SC was injected into 4T1 tumor-bearing mice through tail vein, then its distribution in tumor site and various organs was monitored by fluorescence imaging. As shown in Figure 6A and 6B, following intravenous administration of SC, the fluorescence signal at the tumor site peaked at 4 hours post-injection, then gradually declined before stabilizing between 8-12 hours. Notably, significant fluorescence intensity remained detectable even at 48 hours, demonstrating effective tumor-specific accumulation of SC. As shown in Figure 6C, ex vivo imaging of organs harvested at the 12-hour time point demonstrated predominant SC accumulation in tumor tissue, while substantial amounts were also detected in hepatic and renal tissues. To evaluate the pharmacokinetic behavior of the CSC nanoplatform, blood samples were collected from treated mice at predetermined time intervals. The metabolic clearance of the nanoplatform was assessed by tracking the concentration of the copper element in circulation. Pharmacokinetic analysis revealed a blood circulation half-life ($t_{1/2}$) of 2.78 h for CSC (Figure 6D), demonstrating its gradual elimination from the bloodstream. In summary, CSC achieves prolonged tumor accumulation through enhanced circulatory retention while maintaining efficient

systemic clearance, thus providing a pharmacological foundation for synergistic antitumor therapy.

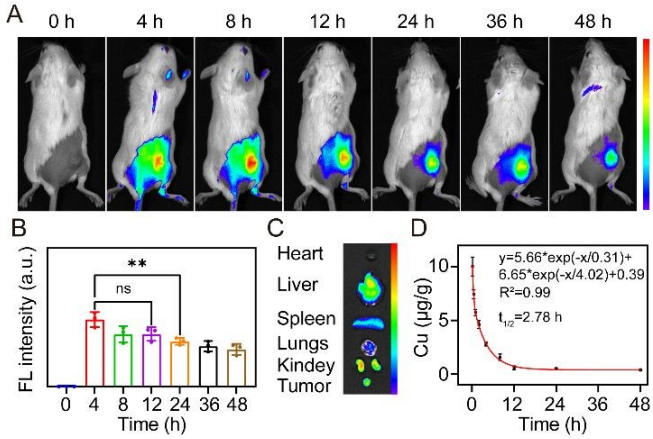

Figure 6. Tumor targeting and metabolism. (A) Fluorescence imaging of tumor at different time points in 4T1 tumor-bearing mice after intravenous of SC. (B) Quantitative Fluorescence Analysis of tumor sites at different time points (n = 3). (C) The distribution of SC nanoplatform in major organs at 12 h. (D) The pharmacokinetics of copper ions during blood circulation over time in healthy mice after injection of CSC (n = 3).

In vivo tumor treatment

We next evaluated the in vivo therapeutic efficacy of CSC nanoplatform in tumor-bearing mice. Female Balb/c mice (4 weeks old) were subcutaneously inoculated with 4T1 cells (10^6 cells), and when tumor volumes reached 80-100 mm^3, the mice were randomly divided into six groups (n=5 per group) for different treatments: (I) PBS, (II) PBS+L, (III) CS, (IV) CS+L, (V) CSC, (VI) CSC+L. During the experiment, body weight and tumor volume were measured every two days to monitor therapeutic effects and potential toxicity.

As shown in Figure 7A, after establishing the subcutaneous breast cancer model, different nanoplatforms were injected, followed by laser irradiation at the 12 th hour post-injection to evaluate the therapeutic efficacy over 18 days. Figure 7B demonstrates that the body weight trends of mice in all groups remained consistent with the blank control group throughout the 18-day period, indicating that the nanoplatform treatments caused no harm to the mice. Tumor volume monitoring (Figure 7C) revealed that neither the PBS group nor the PBS+L group exhibited tumor growth inhibition. In the CS, CS+L, and CSC groups, tumors continued to grow progressively, suggesting no significant therapeutic effect. In contrast, the CSC+L group showed marked suppression of tumor growth, confirming that copper ions alone had limited antitumor efficacy, while their combination with photodynamic therapy (PDT) achieved pronounced therapeutic outcomes. Figure 7D displays tumors excised from mice on day 18, highlighting the long-term therapeutic benefits of the nanoplatform. Furthermore, statistical analysis of tumor volume changes in individual mice over 18 days (Figure 7E) and comparative images of tumors before and after treatment (Figure 7F) provided direct visual evidence of the superior therapeutic performance of the CSC+L group compared to other treatments. These results collectively demonstrate that only the CSC nanoplatform combined with laser irradiation (CSC+L) could effectively inhibit tumor growth, exhibiting statistically significant differences compared to all other groups.

To further evaluate tumor tissue damage post-treatment, TUNEL and HE staining were performed on tumor sections after different therapeutic interventions. As shown in Figure 7G, tumor tissues from the PBS and PBS+L groups exhibited strong blue fluorescence but negligible green fluorescence, indicating minimal cellular damage. In contrast, the CS, CS+L, and CSC groups showed sporadic green fluorescence, suggesting limited apoptosis likely induced by copper ion overload. Notably, the CSC+L group (laser-irradiated CSC) displayed intensive green fluorescence, demonstrating massive apoptosis and confirming the synergistic effect between copper ions and photodynamic therapy. HE staining results (Figure 7H) revealed that control group tumors exhibited characteristic malignant features: densely packed cells with minimal intercellular space, enlarged nuclei, and irregular morphology due to rapid proliferation. In contrast, tumors treated with CSC nanoplatform combined with laser irradiation showed markedly improved histopathology - increased intercellular spacing, reduced cell density, and normalized nuclear morphology, demonstrating effective suppression of tumor growth through combined cuproptosis and photodynamic therapy.

Experimental

Materials

Copper chloride dihydrate ($CuCl_2{\cdot}2H_2O$), sodium hydroxide (NaOH) were purchased from Sinopharm Chemical Reagent Co., Ltd (Shanghai, China). Polyvinylpyrrolidone (PVP), L-ascorbic acid, tetraethyl orthosilicate (TEOS), γ-aminopropyl triethoxysilane (APTES) were purchased from Shanghai Aladdin Biochemical Technology Co., Ltd. Ce6 was purchased from Shanghai Macklin Biochemical Co., Ltd. $mPEG_{5000}$-silane was purchased from GuangZhou Tanshtech Co., Ltd . 2, 7-Dichlorodihydrofluorescein diacetate (DCFH-DA), Calcein acetoxymethyl ester (Calcein AM), propidium iodide (PI), BCA protein assay Kit, SDS-PAGE sample loading buffer, hydrophobic polyvinylidene fluoride (PVDF) were purchased from Beyotime Biotechnology. All reagents were used directly without further purification. Deionized (DI) water (Millipore Milli-Q grade, 18.2 MΩ) was used in all the experiments. Female Balb/c mice were purchased from Beijing Vital River Laboratory Animal Technology Co., Ltd.

Instruments

The morphology of nanoplatform was characterized by HT770 transmission electron microscope (TEM) (Hitachi, Japan). Hydrated particle size and zeta potential of the nanoplatform were measured on Nano-ZS90 nanometer (Malvern, UK). The absorption spectrum was recorded by UV-2550 (UV–vis spectrophotometer (Shimadzu, Japan). The elemental composition of nanoplatform was analyzed by AXISULTRA DLD-600 W X-ray photoelectron spectra (XPS) (Shimadzu, Japan). The concentration of copper was determined by WFX-200 atomic absorption spectrophotometer (Beijing Beifen-Ruili

View Article Online
DOI: 10.1039/D5BM00954E

Analytical Instrument Co., Ltd, China). The fluorescence imaging of cell was acquired with FV3000 confocal microscope (Olympus, Japan). MDL-III-660-2.3 W laser (Changchun New Industries Optoelectronics Tech. Co., Ltd, China) was used for laser irradiation.

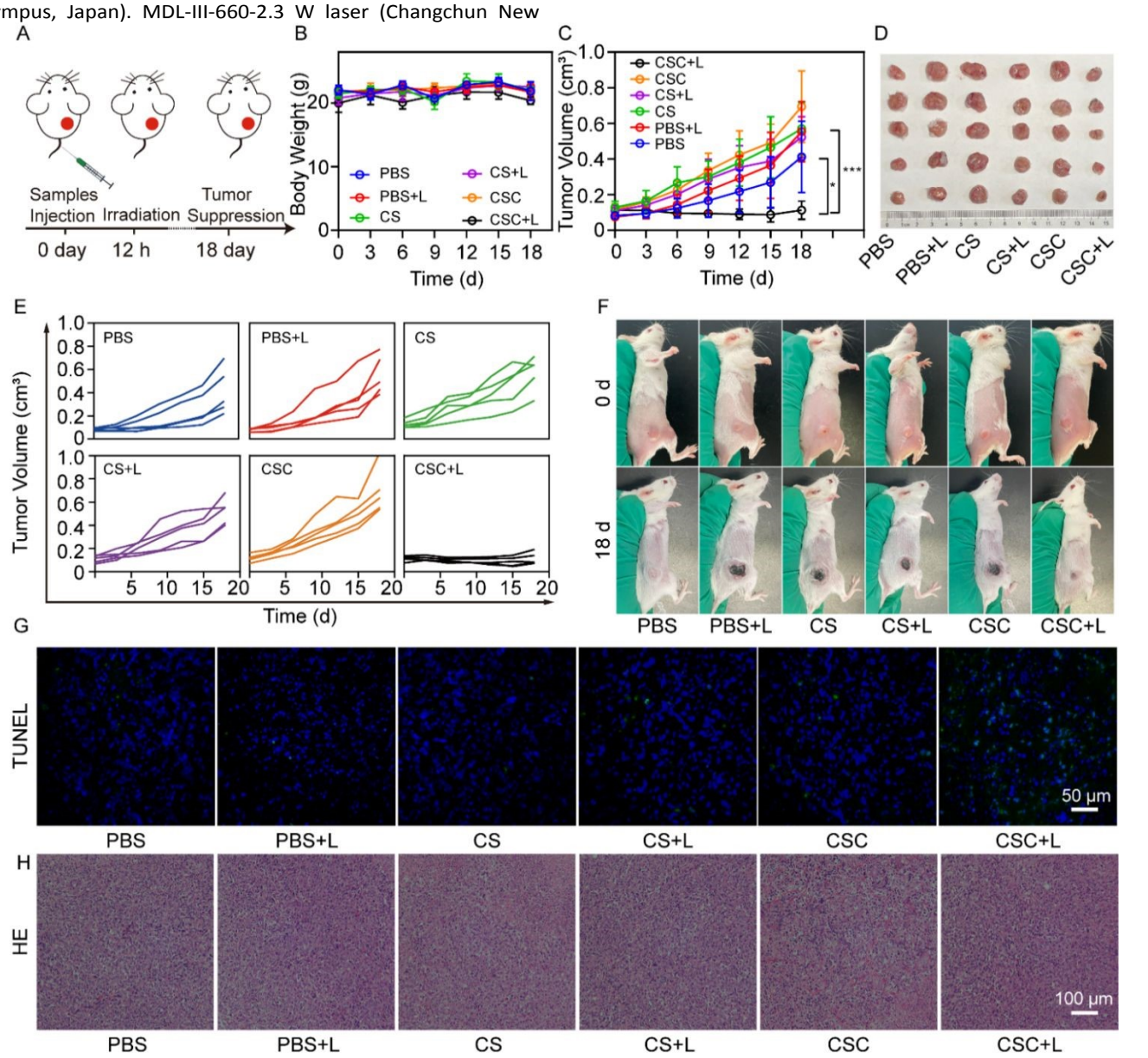

Figure 7. In vivo tumor therapy of CSC. (A) Treatment process. (B) Body weight change. (C) Tumor volume after different treatments. (D) Photographs of representative tumors after different treatments. (E) Tumor volume change curves for each mouse after different treatments. (F) Representative photographs of mice from different groups after various treatments. (G) TUNEL staining of tumor. Scale bar: 50 μm and (H) HE staining of tumor after various treatments. Scale bar: 100 μm. Data were presented as the means ± SD (n = 5 mice per group). *: $p < 0.05$; **:$p < 0.01$; ***: $p < 0.001$.

Synthesis of Cu_2O nanoplatform

$CuCl_2 \cdot 2H_2O$ (0.10 mmol) and PVP (0.10 g) were dissolved in 50.0 mL of deionized water, followed by the dropwise addition of 2.0 mL of 0.2 M NaOH; the solution was stirred magnetically for 5 min. Finally, 2.0 mL of 0.10 M ascorbic acid was added dropwise, and the solution was further stirred for 5 min. The product was recovered by centrifugation and then washed with ethanol twice.

Synthesis of CS

Briefly, Cu_2O particles were redispersed in 40 mL of ethanol by sonication for 30 min. Then, 40 μL of TEOS was added to the mixture and stirred for 10 min. Later, 5 mL of NaOH (8 mM) was added to the above mixture and stirred thoroughly for another 10 min. The resultant mixture was further stirred at room temperature for 12 h before separating the solid phase via centrifugation. The process is carried out under argon shielding throughout. The product (CS) was washed twice with ethanol.

Synthesis of CSC.

CS particles were redispersed in 40 mL of ethanol by sonication for 30 min. Then, 10 mg mPEG-Saline and 40 μL

APTES was added to the above mixture and stirred thoroughly for another 10 min. Later, 5 mL of NaOH (8 mM) was added to the above mixture and stirred for another 6 hours. The product (CS-NH_2) was washed twice with ethanol. CS-NH_2 particles were redispersed in 10 mL of HEPES buffer, a mixed solvent (6 mg of EDC, 4 mg of NHS and 4 mg of Ce6) was added to the above mixture and stirred thoroughly for another 4 hours. The product (CSC) was washed twice with ethanol and then dispersed it in water.

Release of copper ions

A solution of CSC (4 mg mL^{-1}) was placed in a dialysis bag. The pH of the dialysate was then adjusted to 5.5, 6.5, and 7.4. 200 µL of the solution collected at specific time intervals of 5, 10, 30 min and 1, 2, 6, 12, 24,36 h was taken out for detection.

Cellular Uptake

4T1 cell was seeded in confocal dish and cultured overnight, and 1 mL serum-free medium containing CSC (50 µg mL^{-1}) was added and incubated for 1, 2, 4, and 6 h, respectively. After washing with PBS for three times, the cell was stained with DAPI for10 min, and then observed under laser confocal scanning microscopic imaging system. For flow cytometry assay, 4T1 cells was seeded in 6-well plate and incubated overnight, and 1 mL serum-free medium containing CSC (50 µg mL^{-1}) was added and incubated for 1, 2, 4, 6 h respectively. Then, 10000 cells were quantificationally analyzed of Ce6 fluorescence intensity by flow cytometer.

Detection of intracellular protein expression

4T1 cells were seeded into 6-well plates at a density of 1.0 × 10^5 cells per well and cultured in a 5% CO_2 incubator at 37 °C for 12 h. The cells were then treated with PBS, CS or CSC for 12 h. The cell pellet was collected and lysed using RIPA buffer to extract total proteins. Protein concentration was determined using BCA Protein Concentration Assay Kit and samples were adjusted to ensure equal loading amounts. Subsequently, SDS loading buffer was added to the protein samples, followed by heat denaturation at 95 °C for 5–10 minutes. Electrophoresis is then performed using SDS-PAGE gels. After separation, proteins are transferred to PVDF or nitrocellulose membranes using wet transfer systems, with careful attention to proper "sandwich" assembly and transfer conditions. The membranes are subsequently blocked with 5% skim milk or BSA to prevent nonspecific binding before incubation with primary antibodies (typically overnight at 4 °C) and HRP-conjugated secondary antibodies. Following thorough washing steps to remove unbound antibodies, protein bands are visualized using Enhanced Chemiluminescence (ECL) detection systems.

Cytotoxicity assay

4T1 cells and NIH 3T3 cells were respectively inoculated into 96-well plates and cultured in a 5% CO_2 incubator at 37 °C overnight, then the medium was removed, different concentrations of CSC (0, 3.1, 6.3, 12.5, 25, 50, 100 and 200 µg mL^{-1}) were added. After 12 h, the medium was removed, and the cells were washed with PBS three times. Then, 200 µL of CCK-8 solution was added to each well. Subsequently, the absorption at 450 nm of each well was measured using an enzyme marker to determine cell viability.

Detection of Intracellular ROS

DCFH-DA was used to detect intracellular ROS. 4T1 cell was seeded in 6-well plates and cultured overnight, and 2 mL of serum-free medium containing the same concentration of Cu_2O, CS, and CSC (50 µg mL^{-1}) was added and incubated for 4 h. After washing three times with PBS, serum-free medium containing DCFH-DA (10 µM) was added and incubated for 30 min. Afterward, the cell in some groups was irradiated with 660 nm laser (100 mW cm^{-2}) for 3 min in dark and then observed under laser confocal scanning microscopic imaging system.

In Vivo Toxicity Evaluation of CSC

Six-week-old female Balb/C mice were randomly divided into five groups, four groups were injected with 200 µL of CSC (20 mg kg^{-1}) through the tail vein, and the last group was injected with the same amount of PBS as control. After 1, 7, 14 and 30 d of observation, the mice were sacrificed and blood was collected for blood routine and biochemical determination. In addition, the major organs of heart, liver, spleen, lungs, and kidneys of each group were fixed with 4% paraformaldehyde, and embedded in paraffin, and sliced for HE staining. All animal surgeries were performed in accordance with the Guidelines of Assessment for Humane Endpoints in Animal Experiments (Certification and Accreditation Administration of the P. R. China, RB/T 173-2018) and approved by the Ethics Committee for Animal Experimentation of Huazhong University of Science and Technology (No. 4208).

In Vivo Synergistic Treatment Effect Evaluation of CSC

The subcutaneous tumor model was established by injecting about 1 × 10^6 4T1 cells per mouse into the lower right back of Balb/c mice. And the mice bearing 4T1 tumor was randomly divided into 6 groups with 5 mice in each group, including I) PBS, II) PBS+L, III) CS, IV) CS+L, V) CSC, VI) CS+L. After injecting different nanoplatforms (20 mg kg^{-1}) through tail vein for 12 h, II, IV and VI groups were irradiated with 660 nm laser (1 W cm^{-2}) for 6 min, and the temperature change was recorded by near-infrared thermal image. In addition, one mouse in each group was euthanized and the tumor was collected. After washing several times with PBS, it was immersed in 4% paraformaldehyde and fixed for HE and TUNEL staining, respectively. At the same time, the weight and tumor volume of each mouse in every group were recorded by digital vernier caliper and scale every other day. After 18 d, the mice were euthanized, and the tumor was dissected and weighed to calculate the tumor mass and tumor suppression rate.

Conclusions

In this study, we successfully developed a nanotherapeutic probe (CSC) by integrating cuprous oxide (Cu_2O) and Ce6 photosensitizer for combined photodynamic therapy (PDT) and cuproptosis in breast cancer treatment. The nanoplatform accumulated at the tumor site through the enhanced permeability and retention (EPR) effect. Under external laser irradiation, the photosensitizer Ce6 generated substantial

reactive oxygen species (ROS). Simultaneously, the acidic tumor microenvironment triggered the degradation of Cu_2O nanoplatform, releasing abundant copper ions. These ions entered cells, bound to lipoylated proteins, and induced their aggregation, thereby disrupting mitochondrial metabolism and triggering cuproptosis. Experimental results demonstrated significant synergistic therapeutic effects between PDT and cuproptosis.

Author contributions

Yong-Guo Hu and Fang Zhang designed the project, performed the experiments and wrote the original manuscript. Fang Zhang and Li-Li Chen analyzed the results. Xin-Yue Xu, Pei-Jie Zhang and Yong Li investigated relevant literature. Jin-Xuan Fan, Jia-Hua Zou and Yuan-Di Zhao provided useful advice for this work.

Conflicts of interest

The authors declare no competing interests.

Data availability

The authors confirm that the data supporting the findings of this study are available within the article and its ESI.

Acknowledgements

This work was supported by the National Natural Science Foundation of China (Grant No. 62375093), Technology Innovation Program of Hubei Province (2024BCB058), the Natural Science Foundation of Hubei Province of China (2025AFB559), China Ageing Development Foundation - Elderly Navigation Program Research Fund (193). We also thank the Analytical and Testing Center (HUST), the Research Core Facilities for Life Science (HUST) for the help of measurement.

References

1. Y. You, Z. Guo, T. Wolter and Q. Hu, *Chem. Soc. Rev.,* 2025, **54**, 1552-1582.
2. R. Joshi, B. Telang, G. Soni and A. Khalife, *Oncol. Transl. Med.,* 2024, **10**, 105-109.
3. I. Poon, C. Lucas, A. Rossi and K. Ravichandran, *Nat. Rev. Immunol*., 2014, **14**, 166-180.
4. Y. Huang, C. Lee, P. Borgström and R. A. Gjerset, *Mol. Ther.,* 2007, **15**, 524-533.
5. J. Zhang, Y. Hu, X. Wen, Z. Yang, Z. Wang, Z. Feng, H. Bai, Q. Xue, Y. Miao, T. Tian, P. Zheng, J. Zhang, J. Li, L. Qiu, J. Xu and D. Ye, *Nat. Nanotechnol.*, 2025, **20**, 563-574.
6. J. Inkol, M. Westerveld, S. Verburg, S. Walsh, J. Morrison, K. Mossman, S. Worfolk, K. Kallio, N. Phippen, R. Burchett, Y. Wan, J. Bramson and S. Workenhe, *J. Immunother. Cancer*, 2024, **12**, e006781.
7. P. Tsvetkov, S. Coy, B. Petrova, M. Dreishpoon, A. Verma, M. Abdusamad, J. Rossen, L. Joesch-Cohen, R. Humeidi, R. Spangler, J. Eaton, E. Frenkel, M. Kocak, S. Corsello, S. Lutsenko, N. Kanarek, S. Santagata and T. Golub, *Science*, 2022, **375**, 1254-1261.
8. L. Chen, J. Min and F. Wang, *Signal. Transduct. Tar*., 2022, **7**, 378.
9. W. Wang, W. Mo, Z. Hang, Y. Huang, H. Yi, Z. Sun and A. Lei, *ACS Nano*, 2023, **17**, 19581-19599.
10. P. Tsvetkov, A. Detappe, K. Cai, H. Keys, Z. Brune, W. Ying, P. Thiru, M. Reidy, G. Kugener and J. Rossen, *Nat. Chem. Biol.*, 2019, **15**, 681-689.
11. R. Lill and S. Freibert, *Annu. Rev. Biochem.*, 2020, **89**, 471-499.
12. X. Zhang, B. Tang, J. Luo, Y. Yang, Q. Weng, S. Fang, Z. Zhao, J. Tu, M. Chen and J. Ji, *Mol. Cancer*, 2024, **23**, 255.
13. F. Hu, J. Huang, T. Bing, W. Mou, D. Li, H. Zhang, Y. Chen, Q. Jin, Y. Yu and Z. Yang, *Adv. Sci.*, 2024, **11**, 2309388.
14. C. Wang, X. Yang, C. Dong, K. Chai, J. Ruan and S. Shi, *Coordin. Chem. Rev.*, 2023, **487**,215156.
15. Z. Li, J. Yang, B. Ren, Q. Fan, L. Huang, S. Guo, R. Zhou, S. Chen, J. Feng, C. Yan, X. Chen and Z. Shen, *Adv. Mater.*, 2024, **36**, 2313212.
16. S. Ning, M. Lyu, D. Zhu, J. W. Y. Lam, Q. Huang, T. Zhang and Z. Tang, *ACS Nano*, 2023, **17**, 10206-10217.
17. Y. Wang, X. Yao, Y. Lu, J. Ruan, Z. Yang, C. Wang, N. Yang, Y. Gao and S. Shi, *Adv. Mater.*, 2025, **21**, 2501435.
18. M. Guan, K. Cheng, X. Xie, Y. Li, M. Ma, B. Zhang, S. Chen, W. Chen, B. Liu, J. Fan and Y. Zhao, *Nat. Commun.*, 2024, **15**, 10060.
19. H. Xiang, C. You, W. Liu, D. Wang, Y. Chen and C. Dong, *Biomaterials*, 2021, **277**, 121071.
20. Y. Zhang, S. Ya, J. Huang, Y. Ju, X. Fang, X. Ouyang, Q. Zeng, X. Zhou, X. Yan and G. Nie, *Exploration*, 2025, **5**, 20240275.
21. Y. Ding, Y. Xu, W. Yang, P. Niu, X. Li, Y. Chen, Z. Li, Y. Liu, Y. An, Y. Liu, W. Shen and L. Shi, *Nano Today*, 2020, **35**, 100970.
22. S. Sindhwani, A. Syed, J. Ngai, B. Kingston, L. Maiorino, J. Rothschild, P. MacMillan, Y. Zhang, N. Rajesh, T. Hoang, J. Wu, S. Wilhelm, A. Zilman, S. Gadde, A. Sulaiman, B. Ouyang, Z. Lin, L. Wang, M. Egeblad and W. Chan, *Nat. Mater.*, 2020, **19**, 566-575.
23. L. Wang, J. Piao, H. Qi, C. Qiao, Q. Guo, M. Wei and Z. Li, *Coordin. Chem. Rev.*, 2025, **523**, 216284.
24. C. Zhang, T. Huang and L. Li, *J. Hematol. Oncol.*, 2024, **17**, 68.
25. S. Gao, H. Ge, L. Gao, Y. Gao, S. Tang, Y. Li, Z. Yuan and W. Chen, *Adv. Sci.*, 2025, **12**, 2417676.
26. Y. Li, X. Lei, X. Zhang, B. Zhang, Y. Hu, M. Guan, K. Cheng, W. Chen, B. Liu, J. Fan and Y. Zhao, *Angew. Chem. Int. Ed.*, 2024, **63**, e202411598.
27. J. Fan, M. Peng, H. Wang, H. Zheng, Z. Liu, C. Li, X. Wang, X. Liu, S. Cheng and X. Zhang, *Adv. Mater.*, 2019, **31**, 1808278.
28. S. Sun, Q. Chen, Z. Tang, C. Liu, Z. Li, A. Wu and H. Lin, *Angew. Chem. Int. Ed.*, 2020, **59**, 21041-21048.
29. Z. Yang, X. Shen, J. Jin, X. Jiang, W. Pan, C. Wu, D. Yu, P. Li, W. Feng and Y. Chen, *Adv. Sci*, 2024, **11**, 2400251
30. T. Wu, X. Yan, R. Zhang and K. Fan, *J. Inorg. Mater.*, 2022, 2023, **38**, 43-54
31. C. Wu, Y. You, D. Yu, Y. X. Zhu, H. Lin and J. Shi, *Adv. Healthcare Mater.*, 2025, **14**,2501021.
32. B. Jia, Y. Liu, X. Geng, Y. Li, C. Zhang, Y. Qu, X. Liu, M. Zhao, Y. Yang and W. Li, *Research*, 2025, **8**, 0732.
33. N. Song, H. Li, R. Tao, Y. Huang, R. Zhang, J. Guo, P. Liu, C. Yao and D. Yang, *Adv. Mater.*, 2025, **21**, 2416161.
34. L. Yu, W. Li, J. Cao, R. Miao, Y. Fu, X. Wang, J. Xie, W. Zhang, Z. Mao, H. Zhang, Y. Zhang, M. Ou and L. Mei, *Adv. Funct. Mater.*, 2025, **21**, 2425831.
35. J. Shi, X. Qi, Y. Ran, Q. Zhou, Y. Ding, L. Li, Y. Zeng, D. Qiu, Z. Cai, X. Cai and Y. Pan, *Bioact. Mater.*, 2025, **47**, 212-228.
36. X. Chen, L. Lu, Z. Liang, B. Yu, Z. Shao, J. Li, Y. Cen, Y. Liu, S. Li and X. Chen, *Angew. Chem. Int. Ed.*, 2025, **21**, e202502120.
37. R. Zhou, X. Zeng, H. Zhao, Q. Chen and P. Wu, *Coord. Chem. Rev.*, 2022, **452**, 214306.
38. Y. Liang, Q. Yuan, Q. Zheng, Z. Mei, Y. Song, H. Yan, J. Yang, S. Wu, J. Yuan and W. Wu, *Nucleic Acids Res.*, 2024, **52**, D1218-D1226.

View Article Online
DOI: 10.1039/D5BM00954E

39. K. Sun, X. Wei, S. Han, Y. Sun, H. Xiao and D. Wei, *ACS Nano*, 2025, **19**, 13300-13313.
40. Q. Zhan, Y. Kuang, X. Chen, Y. Yang, L. Jiang, J. Chen, L. Li, J. Wang, S. Zhu and H. Huang, *Bioact. Mater.*, 2025, **47**, 327-342.
41. Y. Zhong, Z. Qiu, K. Zhang, Z. Lu, Z. Li, Y. Cen, S. Li and H. Cheng, *Adv. Mater.*, 2025, **37**, 2415078.
42. G. Zhan, L. Fan, S. Zhou and X. Yang, *ACS Appl. Mater. Interfaces*, 2018, **10**, 35234-35243.
43. C. Yec and H. Zeng, *Chem. Mater.*, 2012, **24**, 1917-1929.
44. S. Dong, Y. Dong, T. Jia, S. Liu, J. Liu, D. Yang, F. He, S. Gai, P. Yang and J. Lin, *Adv. Mater.*, 2020, **32**, 2002439.
45. B. Li, J. Ma and P. Cheng, *Angew. Chem. Int. Ed.*, 2018, **130**, 6950-6953.
46. H. Zhou, Z. Fan, J. Deng, P. Lemons, D. Arhontoulis, W. Bowne and H. Cheng, *Nano Lett.*, 2016, **16**, 3268-3277.
47. Y. Akiyama, T. Mori, Y. Katayama and T. Niidome, *J. Control. Release*, 2009, **139**, 81-84.
48. C. Xue, M. Li, Y. Zhao, J. Zhou, Y. Hu, K. Cai, Y. Zhao, S. Yu and Z. Luo, *Sci. Adv.*, 2020, **6**, eaax1346.

View Article Online
DOI: 10.1039/D5BM00954E

Data availability

The authors confirm that the data supporting the findings of this study are available within the article and its ESI